

# Identical Suppression of Spin and Charge Density Wave Transitions in $\text{La}_4\text{Ni}_3\text{O}_{10}$ by Pressure

Rustem Khasanov,<sup>1,\*</sup> Thomas J. Hicken,<sup>1,†</sup> Igor Plokhikh,<sup>1,‡</sup> Vahid Sazgari,<sup>1</sup> Lukas Keller,<sup>1</sup> Vladimir Pomjakushin,<sup>1</sup> Marek Bartkowiak,<sup>1</sup> Szymon Królak,<sup>2,3</sup> Michał J. Winiarski,<sup>2,3</sup> Jonas A. Krieger,<sup>1</sup> Hubertus Luetkens,<sup>1</sup> Tomasz Klimczuk,<sup>2,3</sup> Dariusz J. Gawryluk,<sup>1</sup> and Zurab Guguchia<sup>1</sup>

<sup>1</sup>*PSI Center for Neutron and Muon Sciences CNM, 5232 Villigen PSI, Switzerland*

<sup>2</sup>*Faculty of Applied Physics and Mathematics, Gdańsk University of Technology, Narutowicza 11/12, Gdansk, 80-233 Poland*

<sup>3</sup>*Advanced Materials Center, Gdańsk University of Technology, Narutowicza 11/12, Gdansk, 80-233 Poland*

Understanding the interplay between magnetism and superconductivity in nickelate systems is a key focus of condensed matter research. Microscopic insights into magnetism, which emerges near superconductivity, require a synergistic approach that combines complementary techniques with controlled parameter tuning. In this paper, we present a systematic investigation of the three-layer Ruddlesden-Popper (RP) nickelate  $\text{La}_4\text{Ni}_3\text{O}_{10}$  using muon-spin rotation/relaxation ( $\mu\text{SR}$ ), neutron powder diffraction (NPD), resistivity, and specific heat measurements. At ambient pressure, two incommensurate spin density wave (SDW) transitions were identified at  $T_{\text{SDW}} \simeq 132$  K and  $T^* \simeq 90$  K. NPD experiments revealed that the magnetic wave vector  $(0, 0.574, 0)$  remains unchanged below 130 K, indicating that the transition at  $T^*$  corresponds to a reorientation of the Ni magnetic moments within a similar magnetic structure. Comparison of the observed internal magnetic fields with dipole-field calculations reveals a magnetic structure consistent with an antiferromagnetically coupled SDW on the outer two Ni layers, with smaller moments on the inner Ni layer. The internal fields at muon stopping sites appeared abruptly at  $T_{\text{SDW}}$ , suggesting a first-order-like nature of the SDW transition, which is closely linked to the charge density wave (CDW) order occurring at the same temperature ( $T_{\text{SDW}} = T_{\text{CDW}}$ ). Under applied pressure, all transition temperatures, including  $T_{\text{SDW}}$ ,  $T^*$ , and  $T_{\text{CDW}}$ , were suppressed at a nearly uniform rate of  $\simeq -13$  K/GPa. This behavior contrasts with the double-layer RP nickelate  $\text{La}_3\text{Ni}_2\text{O}_7$ , where pressure enhances the separation of the density wave transitions.

## I. INTRODUCTION

The exploration of nickelates, including those belonging to the Ruddlesden-Popper (RP) series  $\text{La}_{(n+1)-x}\text{Pr}_x\text{Ni}_n\text{O}_{3n+1}$  ( $n = 2, 3$ ), has garnered significant attention in condensed matter physics and materials science due to their intriguing structural, electronic, and magnetic properties<sup>1–21</sup>. The recent observation of high-temperature superconductivity under high pressure in a member of the RP series with  $n = 2$ , has further enhanced interest in this class of materials, highlighting their potential for groundbreaking discoveries. Relevant studies include recent works on  $\text{La}_{3-x}\text{Pr}_x\text{Ni}_2\text{O}_7$  under high pressure, which demonstrate its superconducting properties,<sup>1,5,12</sup> as well as investigations into the electronic and structural properties of  $\text{La}_{4-x}\text{Pr}_x\text{Ni}_3\text{O}_{10}$ <sup>2,7,12,15–18</sup>. Among these, the compound  $\text{La}_4\text{Ni}_3\text{O}_{10}$ , a member of the RP series with  $n = 3$ , stands out due to its proximity to potential metal-to-metal transitions<sup>8–10,19,20</sup>, charge ordering<sup>2,7</sup>, and unconventional superconductivity<sup>3,4,6</sup>. Such features make it a promising candidate for understanding correlated electron systems and for exploring novel phenomena under extreme conditions.

At ambient pressure,  $\text{La}_4\text{Ni}_3\text{O}_{10}$  exhibits two types of order, namely the charge density wave (CDW) and spin density wave (SDW) states. These states have similar ordering temperatures and are strongly intertwined, highlighting the complex interplay of charge and spin degrees of freedom in this material<sup>2</sup>. Superconductivity was re-

ported in this compound at high pressures, suggesting a rich phase diagram where multiple states compete and coexist. The phase diagram of  $\text{La}_4\text{Ni}_3\text{O}_{10}$  reveals a delicate balance between the CDW/SDW states and the superconducting phase, with pressure acting as a key tuning parameter<sup>3,4,6</sup>. As pressure increases, the suppression of CDW and SDW order appears to coincide with the stabilization of the superconducting state, indicative of the strong interplay between these competing phases.

This paper presents a systematic investigation of  $\text{La}_4\text{Ni}_3\text{O}_{10}$  using a combination of muon-spin rotation/relaxation ( $\mu\text{SR}$ ), neutron powder diffraction (NPD), resistivity, and specific heat experiments. These complementary techniques enable detailed insights into the magnetic and electronic behaviors of the material under varying conditions, particularly at ambient and high pressures. At ambient pressure,  $\text{La}_4\text{Ni}_3\text{O}_{10}$  exhibits two SDW transitions at  $T_{\text{SDW}} \simeq 132$  K and  $T^* \simeq 90$  K. These transitions are accompanied by a magnetic wave vector  $(0, 0.574, 0)$ , which remains unchanged down to the lowest measuring temperatures, suggesting that the transition at  $T^*$  involves a subtle rearrangement of Ni magnetic moments. Under applied pressure, all transition temperatures, including  $T_{\text{SDW}}$ ,  $T^*$ , and  $T_{\text{CDW}}$ , are suppressed, see Fig. 1. Despite this suppression, the SDW and CDW transitions remain closely linked, in contrast to the behavior observed in the two-layer RP nickelate  $\text{La}_3\text{Ni}_2\text{O}_7$ , where pressure enhances the separation between density wave orders<sup>11</sup>. The results underscore the intertwined nature of SDW and CDW orders in  $\text{La}_4\text{Ni}_3\text{O}_{10}$ , consis-

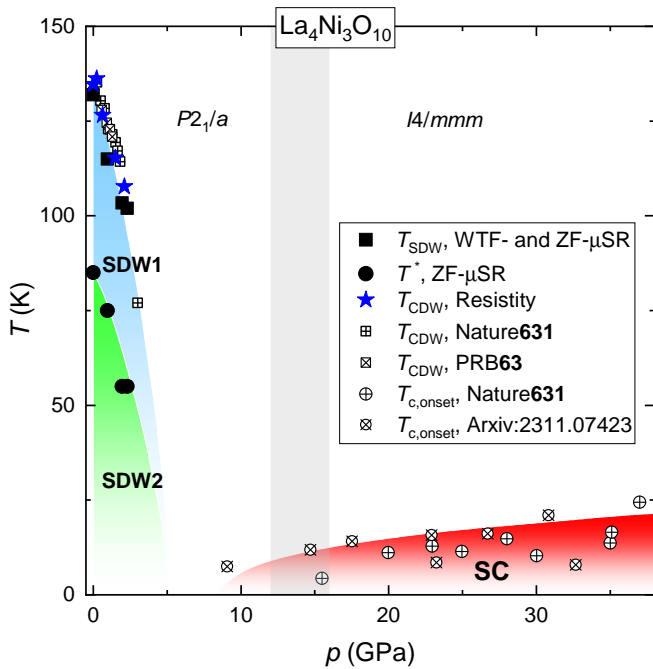


FIG. 1: **The pressure-temperature ( $p - T$ ) phase diagram of  $\text{La}_4\text{Ni}_3\text{O}_{10}$ .** Solid symbols represent the pressure dependencies of the magnetic ordering temperatures  $T_{\text{SDW}}$  and  $T^*$ , as obtained from ZF and WTF- $\mu$ SR experiments (black squares and circles) and the CDW ordering temperature ( $T_{\text{CDW}}$ ) derived from resistivity studies (blue stars) in the present work. The open squares and circles denote the  $T_{\text{CDW}}$  vs.  $p$  and the onset of the superconducting transition temperature  $T_c$  vs.  $p$  data from Refs. 3,6,7.

tent with observations in other correlated systems such as cuprates<sup>22-28</sup> and hole-doped nickelates<sup>29-31</sup>.

## II. AMBIENT PRESSURE STUDIES

This section discusses a series of experiments conducted under ambient pressure conditions, including zero-field muon spin rotation/relaxation, neutron powder diffraction, resistivity, and specific heat measurements.

### A. Sample characterisation

The results of the ambient-pressure characterization of the  $\text{La}_4\text{Ni}_3\text{O}_{10-\delta}$  sample are presented in Figure 2. Fig. 2 (a) shows the x-ray diffraction patterns collected at room temperature. The refinement of the x-ray data yields the monoclinic structure ( $P2_1/a$ , Space Group No. 14) with the lattice parameters  $a = 5.4162(3)$  Å,  $b = 5.4642(2)$  Å,  $c = 27.984(1)$  Å, and  $\beta = 90.256(4)^\circ$ , which is consistent with literature reports<sup>2-4,6,21</sup>.

The oxygen content ( $10-\delta$ ) was determined using thermogravimetric analysis, as shown in Fig. 2 (b). The sample was heated from room temperature to  $1000^\circ\text{C}$  at a

rate of  $1^\circ\text{C}/\text{min}$  and then cooled to room temperature. The total weight loss was attributed to the reduction of fully oxidized  $\text{La}_4\text{Ni}_3\text{O}_{10-\delta}$  to metallic nickel and  $\text{La}_2\text{O}_3$ . The value of  $\delta = 0.01(1)$  was obtained thus suggesting that  $\text{La}_4\text{Ni}_3\text{O}_{10-\delta}$  sample can be considered oxygen stoichiometric. Hereafter, we refer to the studied sample as  $\text{La}_4\text{Ni}_3\text{O}_{10}$ .

The results of resistivity ( $R$ ) and specific heat ( $C_p$ ) measurements are presented in Figs. 2 (c) and (d). The initial  $R(T)$  and  $C_p(T)$  curves exhibit a weak anomaly at  $T \simeq 130$  K, which is associated in the literature with the occurrence of intertwined spin density wave (SDW) and charge density wave (CDW) orders<sup>2,3</sup>. The anomaly becomes more pronounced in the first derivative of the  $R(T)$  data [Fig. 2 (e)] and in the  $C_p/T$  vs.  $T$  curve [Fig. 2 (f)]. Notably, the specific heat data suggest the presence of a second anomaly at  $T^* \simeq 90$  K, which is not observed in resistivity measurements.

### B. Neutron Powder Diffraction data

The high-resolution NPD data were collected at temperatures  $T = 1.7, 100,$  and  $150$  K at HRPT diffractometer and suggest the absence of the structural transition between 1.7 and 150 K [Fig. 3 (a)]. The analysis of the crystal structure is consistent with the  $P2_1/a$  symmetry obtained in x-ray experiments [Fig. 2 (a)].

To visualize the magnetic peaks, the high-intensity NPD patterns collected at DMC diffractometer were analyzed by subtracting pattern measured at  $T \simeq 160$  K from the data obtained at lower temperatures [Fig. 3 (b)]. A broad hump centered at  $2\theta_n \simeq 28^\circ$ , which disappears above approximately 130 K, represents the magnetic response of the  $\text{La}_4\text{Ni}_3\text{O}_{10}$  sample. Considering the observation of incommensurate magnetic peaks at  $(0, q_s, 4n + 2)$  positions ( $n$  is an integer)<sup>2</sup>, this feature can be attributed to the  $(0, q_s, 2)$  peak, with  $q_s = 0.574(5)$  [Fig. 3 (c)]. Notably, this  $q_s$  value is slightly smaller than the previously reported  $q_s \simeq 0.62$  in Ref. 2.

Fitting the magnetic peak with a Gaussian function yields a peak position and full width at half maxima of  $27.8^\circ$  and  $4.0^\circ$  [Fig. 3 (c)], whereas the neighboring nuclear peaks are  $\simeq 1.2^\circ$  broad and are nearly resolution limited. The broadening of the magnetic peak is due to the reduced correlation length ( $\xi_n$ ) of the incommensurate order. From the equation  $\xi_n \simeq \lambda_n/\beta_n \cos \theta_n$  ( $\lambda_n$  is the neutron wavelengths,  $\beta_n$  is the peak broadening, and  $\theta_n$  is the scattering angle, Ref. 32) the averaged correlation length can be estimated to be of the order of  $\xi_n \simeq 80$  Å. This is consistent with the previous report,<sup>2</sup> showing that the correlation length of the charge density wave within the  $ab$  plane is  $\sim 100$  Å, whereas along the  $c$ -axis it reduces to  $\sim 20$  Å.

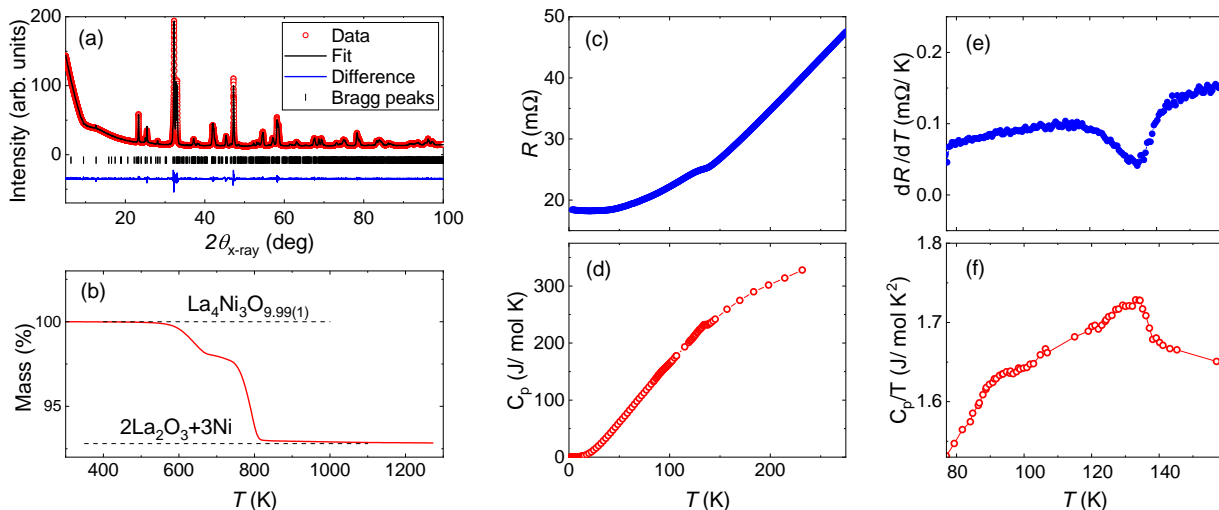


FIG. 2: **Characterization of  $\text{La}_4\text{Ni}_3\text{O}_{10}$  sample.** (a) The x-ray diffraction patterns of  $\text{La}_4\text{Ni}_3\text{O}_{10}$  taken at room temperature. The refinement of the x-ray data yields the monoclinic structure ( $P2_1/a$ , Space Group No. 14). (b) The thermogravimetric curve of the  $\text{La}_4\text{Ni}_3\text{O}_{10-\delta}$  sample, indicating an oxygen content of  $10 - \delta = 9.99(1)$ . (c) Temperature dependence of resistivity  $R(T)$ . (d) Temperature dependence of specific heat  $C_p(T)$ . (e) First derivative of  $R(T)$ . (f)  $C_p(T)/T$ .

### C. Zero-field $\mu\text{SR}$

The zero-field (ZF)  $\mu\text{SR}$  response of  $\text{La}_4\text{Ni}_3\text{O}_{10}$  measured at temperatures  $T = 5$  and  $110$  K is presented in Figs. 4 (a)-(d). Panels (a) and (b) display the ZF asymmetry spectra, which represent the time evolution of the muon-spin polarization, while panels (c) and (d) show the Fourier transform of the data, illustrating the distribution of internal fields. Evidently, the time spectra and magnetic field distributions differ significantly between high and low temperatures. The number of peaks in the field distribution changes from five at  $T = 5$  K [Fig. 4 (c)] to two at  $T = 110$  K [Fig. 4 (d)]. The evolution of the magnetic field distribution is better visualized in the waterfall graph [Fig. 4 (e)], which shows that the five-peak structure transitions to a two-peak one at temperatures between  $90$  K and  $100$  K. Remarkably, this temperature range coincides with the appearance of a second anomaly in the specific heat data [Fig. 2 (f)], thus suggesting that the transformation of the magnetic structure at  $T \simeq 90 - 100$  K is bulk in origin.

Analysis revealed that the ZF- $\mu\text{SR}$  time-spectra cannot be fitted using simple cosine-type oscillating functions, which are typically used to describe a commensurate magnetic order<sup>11,33-35</sup>. Instead, the magnetic field distributions shown in Figs. 4 (c) and (d) suggest the presence of long tails extending from the peak positions to approximately zero field. This feature is characteristic of incommensurate magnetic order, which is typically described by an Overhauser type distribution within the field domain and by a zeroth-order Bessel function ( $J_0$ ) within time domain<sup>36-39</sup>.

The fit of the ZF- $\mu\text{SR}$  data was performed using Eq. 2. The magnetic (m) and nonmagnetic (nm) components, with corresponding weights  $f_m$  and  $1 - f_m$ , were de-

scribed using Eqs. 3 and 4, respectively. The magnetic term (Eq. 3) required the presence of 6 components (5 oscillating and 1 fast relaxing) for the low-temperature data ( $T \lesssim 90$  K), and 3 components (2 oscillating and 1 fast relaxing) for the high-temperature data ( $T \gtrsim 90$  K).

The temperature evolution of magnetic volume fractions ( $f_1$  to  $f_6$ ) is shown in Fig. 4 (f). The total magnetic fraction  $f_m$  represents the sum of individual  $f_i$  components ( $f_m = \sum f_i$ ). The solid line corresponds to the fit<sup>40</sup>:

$$f_m(T) = f_m(0) \left[ 1 + \exp\left(\frac{T - T_{\text{SDW}}}{\Delta T_{\text{SDW}}}\right) \right]^{-1}, \quad (1)$$

where  $f_m(0)$  and  $\Delta T_{\text{SDW}}$  represent the zero-temperature value of the magnetic fraction and the width of the SDW transition, respectively. The fit yields  $f_m(0) = 0.98(1)$ ,  $T_{\text{SDW}} = 131.8(4)$  K, and  $\Delta T_{\text{SDW}} = 3.8(3)$  K. Consequently, below the SDW transition, nearly 100% of the sample response is attributed to the magnetic contribution. The sharpness of the magnetic transition [ $\Delta T_{\text{SDW}} = 3.8(3)$  K] suggests that magnetism in  $\text{La}_4\text{Ni}_3\text{O}_{10}$  sets in homogeneously.

The temperature dependence of the internal fields ( $B_{\text{int},1}$  to  $B_{\text{int},5}$ ) is shown in Fig. 4 (g). Two transitions, corresponding to changes in the internal fields at  $T^* \simeq 90$  K and  $T_{\text{SDW}} \simeq 132$  K, are clearly visible. The first transition at  $T \simeq T_{\text{SDW}}$  is characterized by the abrupt appearance of internal fields at  $B_{\text{int}} \sim 100$  mT. This indicates that the magnetic transition at  $T_{\text{SDW}} \simeq 132$  K is first-order-like and is likely driven by a different type of ordering, such as a structural transition (as observed in CrAs, Refs. 41,42) or a nematic transition (as seen in Fe-based superconductors, Ref. 43). In  $\text{La}_4\text{Ni}_3\text{O}_{10}$ , two density wave transitions, namely spin density wave and charge density wave, occur simultaneously, as reported

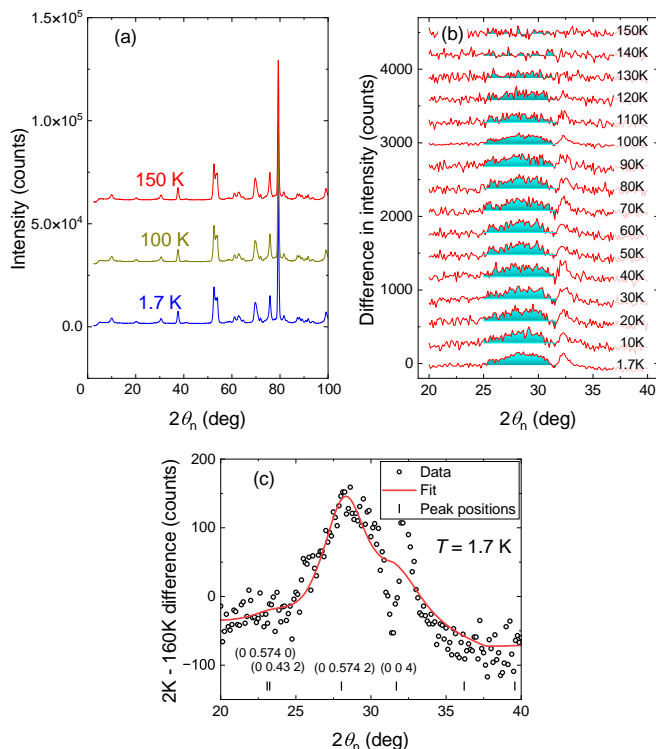


FIG. 3: **Results of neutron powder diffraction experiments.** (a) Diffraction patterns collected at temperatures of 1.7, 100, and 150 K at the HRPT neutron diffractometer ( $\lambda_n = 2.45$  Å).<sup>44</sup> (b) NPD spectra collected at temperatures ranging from 1.7 to 150 K after subtracting the data taken at  $T = 160$  K. Experiments were performed at DMC diffractometer ( $\lambda_n = 3.82$  Å).<sup>45</sup> The broad colored hump corresponds to the magnetic peak. (c) The magnetic peak at  $T = 1.7$  K. The red line represents the fit, identifying the magnetic peak at (0, 0.574, 2). A sharp feature at  $2\theta_n \simeq 32^\circ$  is an artifact from the subtraction of the high-temperature pattern.

in Ref. 2. This suggests that the CDW transition is the primary one, with charge separation initiating the SDW transition.

The second magnetic transition at  $T^* \simeq 90$  K is characterized by a change in the magnetic field distribution from a two-peak to a five-peak structure. Neutron data suggest that the magnetic propagation vector (0, 0.574, 0) remains unchanged across the 90 K temperature range [Fig. 3 (b)]. Thus, changes in the magnetic structure are likely marginal.

Note, that the magnetic transitions at  $T_{SDW}$  and  $T^*$  can be identified using different sets of fitting parameters.  $T_{SDW}$  is best determined from the temperature evolution of the magnetic volume fraction  $f_m$  [Fig. 4 (f)]. In contrast,  $B_{int,i}(T)$  [Fig. 4 (g)] does not approach zero due to the first-order nature of the magnetic transition. Conversely,  $T^*$  is not reflected in the volume fraction dependencies but is associated with the loss of three out of five internal field components for temperatures exceeding 90 K. These magnetic transitions are represented by the

Muon site	Energy (eV)	Coordinates
I	0	(0.396, 0.904, 0.940)
II	0.18	(0.204, 0.790, 0.530)
III	0.22	(0.390, 0.696, 0.999)

TABLE I: The three identified muon stopping sites in  $\text{La}_4\text{Ni}_3\text{O}_{10}$ . The energies are given with respect to the lowest energy calculation. Fractional coordinates are given in terms of the conventional unit cell.

pink and gray vertical lines in Figs. 4 (f) and (g).

To understand the spectra in Fig. 4 (c) and (d), we have calculated the muon stopping site in  $\text{La}_4\text{Ni}_3\text{O}_{10}$ , identifying three distinct sites, given in Table I. Although these three sites have a range of energies, all three could be occupied and show negligible displacement of the surrounding lattice, suggesting the muon is likely to be a faithful probe of the system. Each site sits in a different layer of the material, close to the Ni trilayer structure, as shown in Fig. 5 (a). All three muon sites are between 0.8 and 1 Å from the nearest O atom, as is often found. The lowest energy site sits in the La plane, the highest energy site sits in the plane with the inner Ni layer, and the middle energy site sits in a plane between the other two sites.

We have calculated the dipole field at the muon stopping site assuming all three muon sites are equally occupied. Note that very similar field distributions are produced by just considering the two lower-energy muon sites, therefore we cannot be certain whether or not the third site is occupied. Further we assume that there is no contribution to the spectra from the contact hyperfine interaction that would arise from overlap between the electronic and muon spin wavefunctions; this is consistent with our work on  $\text{La}_3\text{Ni}_2\text{O}_7$ <sup>11</sup>. As the magnetic structure is not fully understood, we have taken the structure proposed in Ref. 2 as a starting point, with an antiferromagnetically-coupled spin density wave on the outer two Ni layers, using the  $q$ -vector obtained in our NPD measurements. Whilst this reproduces many of the features seen in the experiment, we find that this structure gives too much weight to fields near zero; to resolve this, we introduce a small moment on the inner Ni layer. As  $\mu\text{SR}$  is not a  $q$ -resolved probe, we cannot categorically determine the ordering in this layer, hence we make the simplest assumption that the inner layer is also a SDW with the same wavevector, with a phase offset of  $90^\circ$  from both outer layers, as shown in Fig. 5 (b). We use a maximum moment of  $2.81 \mu_B$  on the outer Ni layers, consistent with the full moment of Ni, and the inner moment scaled to  $\sim 8\%$  of this value, as predicted by DFT calculations<sup>46</sup>.

Considering first the situation where the moments point in the  $b$ -direction, as predicted in Ref. 2, our simulations qualitatively resemble the experimental data above 90 K, as shown in Fig. 5 (d). The majority of muons experience a low internal field, with the remainder contributing to a continuous distribution, peaking maxi-

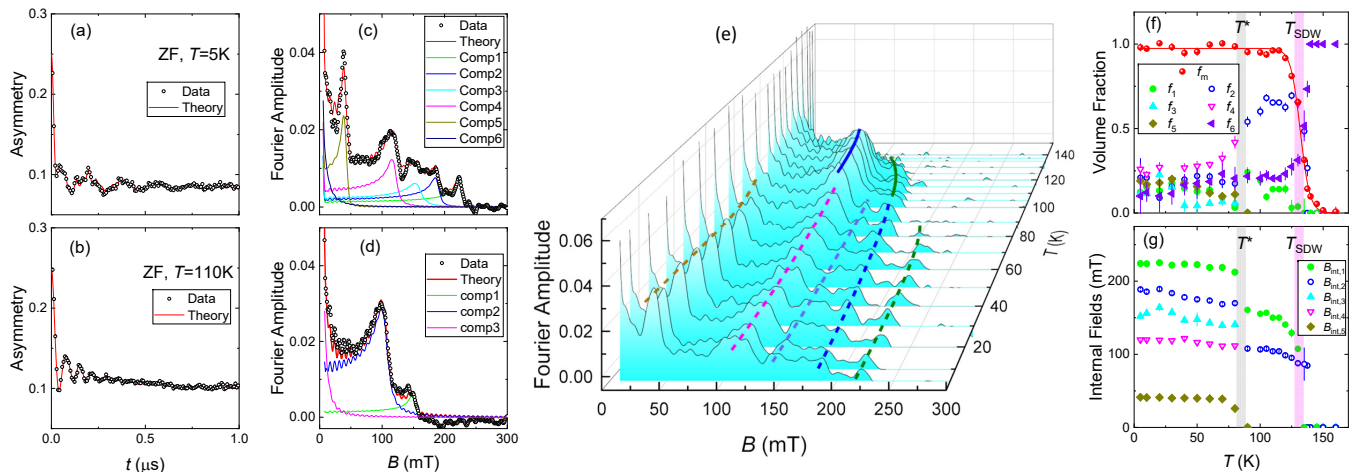


FIG. 4: **Results of ambient-pressure ZF- $\mu$ SR experiments.** (a) and (b) Zero-field  $\mu$ SR time spectra of the  $\text{La}_4\text{Ni}_3\text{O}_{10}$  sample collected at temperatures  $T = 5$  K [panel (a)] and at  $T = 110$  K [panel (b)]. (c) and (d) Fourier transforms of the data presented in panels (a) and (b). Lines represent the fit (red line) and individual fit components. (e) Temperature evolution of the Fourier transform spectra, showing the transition of the magnetic field distribution from a 5-peak to a 2-peak structure. (f) Temperature dependence of ZF- $\mu$ SR signal fractions. The solid line corresponds to a fit of Eq. 1 to  $f_m(T)$ . (g) Temperature dependencies of the internal fields. The gray and pink lines in panels (f) and (g) indicate the positions of the magnetic ordering temperatures  $T^*$  and  $T_{\text{SDW}}$ , respectively. The displayed error bars for parameters obtained from  $\mu$ SR data represent one standard deviation from the  $\chi^2$  fits.

mally around 150 mT. This suggests that at high- $T$ , the magnetic structure is that of coupled SDWs, with the magnetic moments pointing in the  $ab$ -plane, and a smaller moment on the inner Ni layer. At low- $T$  the spectra exhibit additional peaks, suggesting the field at the muon site becomes more varied. There are myriad ways to break this degeneracy, we have considered two key scenarios. (1) Increasing moment on the inner Ni layer. This leads to many more peaks in the spectra, but leaves very little weight at lower magnetic fields, and therefore seems inconsistent with the experimental data. (2) Canting the moments out of the  $ab$ -plane. There are many ways that this could occur, so we have considered the simplest case of rotating all the moments in the same way. We show in Fig. 5 (c) the result when all the moments are rotated  $\theta = 20^\circ$  towards the  $c$ -axis. This produces a qualitatively good match with the experimental data [Figs. 4 (c) and (d)], with the key features all reproduced with approximately the correct weighting. As for  $\theta = 0^\circ$ , the absolute magnitude of the internal field is not correct at lower fields, suggesting that, whilst the main features of the magnetic structure are well explained, there are some subtle details that a  $q$ -resolved probe will be best placed to explore. Our two key results are that (1) there is likely a small magnetic moment on the inner Ni layers, and (2) that it is most likely that the moments lie in the  $ab$ -plane above 90 K, before subtly distorting, gaining a  $c$ -axis component at lower  $T$ .

### III. EXPERIMENTS UNDER HYDROSTATIC PRESSURE

This section discusses the muon-spin rotation/relaxation and resistivity experiments conducted under pressures up to  $\simeq 2.3$  GPa.

#### A. Results of $\mu$ SR experiments

In  $\mu$ SR experiments conducted under pressure, a significant fraction of muons (approximately 50%) stop in the pressure cell walls, contributing to the  $\mu$ SR response as background. Fitting the  $\mu$ SR data under pressure using Eq. 2 requires knowledge of the background contribution from the pressure cell, which was determined in a separate set of experiments<sup>48</sup>. The analysis of ZF- $\mu$ SR under pressure data was performed using Eqs. 2, 3, and 4. The  $\mu$ SR experiments conducted in a weak transverse field ( $B_{\text{WTF}} = 5$  mT), *i.e.*, with a field applied perpendicular to the initial muon-spin polarization, were analyzed using Eq. 2, with the sample part described by Eq. 5.

The temperature dependence of the magnetic volume fraction, obtained from WTF experiments at pressures of  $p = 0.0$  and 1.95 GPa, is shown in Figs. 6 (a) and (b). Solid lines represent fits of Eq. 1 to the  $f_m(T)$  data. Temperature dependencies of internal fields at  $p = 0.0$  and 1.95 GPa, derived from fits to ZF- $\mu$ SR data, are shown in Figs. 6 (c) and (d). The magnetic ordering temperatures  $T^*$  and  $T_{\text{SDW}}$  are indicated by gray and pink vertical lines.

The pressure dependencies of  $T_{\text{SDW}}$ , as determined



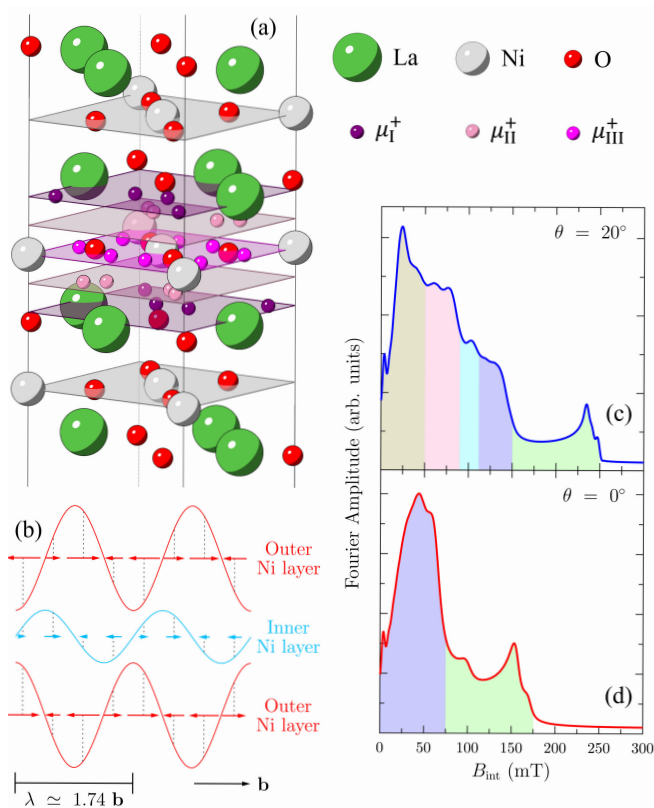


FIG. 5: **Muon stopping site calculations.** (a) The three muon stopping sites are shown, with their relation to the Ni trilayer structure. Symmetrically equivalent positions are all shown, although in the experiment only one position is occupied at any one time. (b) The magnetic structure used in simulations of the ZF  $\mu$ SR spectra. There is a large moment on the outer Ni layers, with a small one on the inner Ni layer. All moments point in the  $b$  direction, and form a SDW. There is a phase shift of  $90^\circ$  between each layer. (c) and (d) Simulations of the dipole field at the muon stopping sites with the moments either pointing in the  $ab$ -plane ( $\theta = 0^\circ$ ), or rotated towards the  $c$ -axis ( $\theta = 20^\circ$ ). Colours under the curves correspond to the colours of the different fit components in Fig. 4 (c) and (d), highlighting the qualitative similarity.

from WTF- $\mu$ SR data, and  $T^*$ , obtained from changes in the magnetic field distribution from the five-peak to the two-peak structure in ZF- $\mu$ SR data, are presented in Fig. 6 (e). Solid lines represent linear fits:  $T_{\text{SDW}}(p) = 131.1(8) \text{ K} - p \cdot 13.1(7) \text{ K/GPa}$  and  $T^*(p) = 86(3) \text{ K} - p \cdot 14(2) \text{ K/GPa}$ , suggesting that both  $T_{\text{SDW}}$  and  $T^*$  decrease with increasing pressure at a nearly equal rate of  $\simeq -13 \text{ K/GPa}$ .

The pressure dependence of internal fields ( $B_{\text{int},1}$  to  $B_{\text{int},5}$ ) measured at  $T = 20 \text{ K}$  is shown in Fig. 6 (f). Typically, the internal field at the muon-stopping site is proportional to the value of the ordered magnetic moments, *i.e.*, to the magnetic moments of Ni ions in our case. However, in  $\text{La}_4\text{Ni}_3\text{O}_{10}$ , the situation appears more complex. Linear fits of  $B_{\text{int},i}(p)$ 's reveal that three internal fields ( $B_{\text{int},1}$ ,  $B_{\text{int},2}$ , and  $B_{\text{int},5}$ ) decrease with pressure

at a similar rate,  $d \ln B_{\text{int},i}/dp \simeq -0.018(5) \text{ GPa}^{-1}$ . In contrast,  $B_{\text{int},3}$  remains nearly constant [ $d \ln B_{\text{int},3}/dp = 0.003(10) \text{ GPa}^{-1}$ ], while  $B_{\text{int},4}$  decreases six times faster [ $d \ln B_{\text{int},4}/dp = -0.128(10) \text{ GPa}^{-1}$ ]. This suggests that pressure not only reduces the value of ordered magnetic moments, which would result in a similar pressure evolution for all internal fields, but may also lead to slight rearrangements of magnetic moments, causing different pressure dependencies for  $B_{\text{int},3}$  and  $B_{\text{int},4}$ . Further studies, particularly precise determinations of the magnetic structure at various pressures, are needed to explain this observation.

## B. Results of Resistivity measurements

The results of resistivity measurements at pressures ranging from 0.22 to 2.1 GPa are presented in Fig. 7. The anomaly in the  $R(T)$  data, which is associated in the literature with the appearance of the CDW ordered state, is visible at low pressures but nearly vanishes at  $p \simeq 2.1 \text{ GPa}$  [Fig. 7 (a)]. The data suggest that pressure suppresses both, the onset of CDW transition and the associated anomaly in  $R(T)$  curves. To make CDW feature more apparent, Fig. 7 (b) shows the first derivatives of the  $R(T)$  data. The ‘dip’ in  $dR(T)/dT$  curves was associated with the CDW transition, and it is marked by red points in Fig. 7 (b).

The pressure dependence of  $T_{\text{CDW}}$  is shown in Fig. 7 (c). The solid line corresponds to a linear fit with  $T_{\text{CDW}}(p) = 135.1(8) \text{ K} - p \cdot 13(2) \text{ K/GPa}$ . For comparison, the  $T_{\text{SDW}}$  transition points, as determined from WTF- $\mu$ SR experiments, are also included in the graph. The data in Fig. 7 (c) reveal that both transition temperatures remain consistent within the error range and exhibit similar pressure dependencies.

## IV. CONCLUSIONS AND OUTLOOK

This study investigates the three-layer Ruddlesden-Popper nickelate  $\text{La}_4\text{Ni}_3\text{O}_{10}$  using  $\mu$ SR, resistivity, specific heat, and neutron powder diffraction, offering comprehensive insights into spin and charge orders interplay under ambient and high-pressure conditions.

At ambient pressure, two distinct density wave orders, charge density wave (CDW) and spin density wave (SDW), were detected. NPD experiments revealed a magnetic peak below 140 K, confirming the presence of SDW order.  $\mu$ SR studies identified the SDW transition at  $T_{\text{SDW}} \simeq 132 \text{ K}$  and suggested a second magnetic transition at  $T^* \simeq 90 \text{ K}$ . Importantly, the magnetic wave vector  $(0, q_s, 0)$ , with  $q_s = 0.574(5)$ , remained unchanged across the two magnetically ordered states, with the transition at  $T^*$  most likely attributed to a subtle change of the magnetic structure.

The incommensurate nature of the SDW-ordered state was established through both NPD and  $\mu$ SR

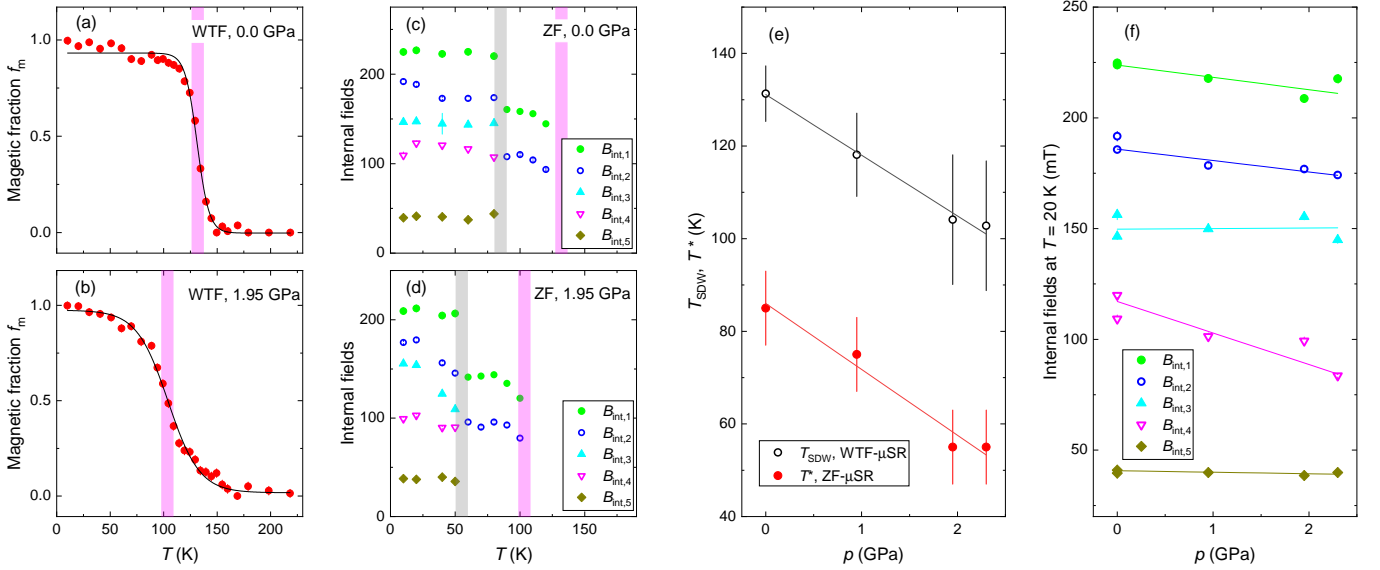


FIG. 6: **Results of WTF and ZF- $\mu$ SR under pressure experiments.** (a) and (b) Temperature dependence of the magnetic volume fraction  $f_m$  measured in WTF- $\mu$ SR experiments at pressures  $p = 0.0$  GPa [panel (a)] and  $p = 1.95$  GPa [panel (b)], respectively. The solid lines represent fits of Eq. 1 to the data. (c) and (d) Temperature evolution of internal fields measured using ZF- $\mu$ SR at  $p = 0.0$  GPa [panel (c)] and  $p = 1.95$  GPa [panel (d)]. The gray and pink lines in panels (a)–(d) indicate the positions of the magnetic ordering temperatures  $T^*$  and  $T_{\text{SDW}}$ . (e) Pressure dependence of the magnetic ordering temperatures  $T^*$  and  $T_{\text{SDW}}$ . (f) Pressure dependence of the internal field components measured in ZF- $\mu$ SR experiments at  $T = 20$  K. The solid lines are linear fits. The displayed error bars for parameters in panels (a)–(d) and (f) are derived from fits of WTF and ZF- $\mu$ SR data and correspond to one standard deviation from the  $\chi^2$  fits. The error bars for the  $T_{\text{SDW}}$  transition represent the SDW transition width ( $\Delta T_{\text{SDW}}$ ) obtained from fitting Eq. 1 to  $f_m(T)$ . Errors for  $T^*$  are estimated as half the temperature step between the nearest measurement points, which were statistically better fitted to either a 5-peak or 5-peak models.

experiments. An incommensurate magnetic peak at  $(0, 0.574, 2)$  was observed, along with an Overhauser-type magnetic field distribution in the field domain (corresponding to a zeroth-order Bessel function in the time domain). Zero-field  $\mu$ SR experiments demonstrated an abrupt change in the internal fields at  $T_{\text{SDW}}$ , consistent with a first-order-like magnetic transition.

The muon stopping sites and dipole-field calculations suggest the possible presence of a small magnetic moment on the inner Ni layers and indicate that the moments likely lie in the  $ab$ -plane above  $T^*$ , before subtly distorting and acquiring a  $c$ -axis component at lower temperatures.

Specific heat measurements revealed distinct anomalies at  $T_{\text{SDW}}$  and  $T^*$ , supporting the bulk nature of these transitions. Additionally, the CDW order was evidenced by an anomaly in the resistivity curve, with  $T_{\text{CDW}}$  coinciding with  $T_{\text{SDW}}$ , consistent with previous studies<sup>2</sup>.

Under applied pressure, the resistivity and  $\mu$ SR experiments revealed the suppression of all transitions, including the two magnetic transitions ( $T_{\text{SDW}}$  and  $T^*$ ) and the CDW transition. The pressure coefficients for these transitions are nearly the same  $\simeq -13$  K/GPa, and the SDW and CDW transitions remained closely intertwined under increasing pressure. The phase diagram constructed from these results is presented in Fig. 1, highlighting

the suppression of density wave transitions with pressure. This behavior contrasts with the two-layer RP nickelate  $\text{La}_3\text{Ni}_2\text{O}_7$ <sup>11</sup>, where external pressure enhanced the separation between SDW and CDW transitions, whereas in  $\text{La}_4\text{Ni}_3\text{O}_{10}$ , these transitions remain closely linked.

The simplest explanation for the different pressure responses of  $\text{La}_3\text{Ni}_2\text{O}_7$  and  $\text{La}_4\text{Ni}_3\text{O}_{10}$  can be formulated as follows: In  $\text{La}_3\text{Ni}_2\text{O}_7$ , the decoupling of the SDW and CDW orders allows the SDW transition to be independently enhanced under pressure. Applying pressure may strengthen the exchange interactions between nearest Ni moments by compressing the lattice, which, in turn, increases the SDW transition temperature. In contrast, in  $\text{La}_4\text{Ni}_3\text{O}_{10}$ , the SDW and CDW orders are strongly coupled and intertwined,<sup>2</sup> meaning the SDW transition is highly dependent on the stability of the CDW. As pressure weakens the CDW order, it also destabilizes the SDW, resulting in a decrease in the SDW transition temperature. This contrast highlights the importance of the coupling between SDW and CDW orders in determining their pressure dependence, with  $\text{La}_4\text{Ni}_3\text{O}_{10}$  exhibiting mutual destabilization under pressure, while  $\text{La}_3\text{Ni}_2\text{O}_7$  benefits from more independent behavior of the SDW.

The relationship between spin and charge orders in  $\text{La}_4\text{Ni}_3\text{O}_{10}$  mirrors the intricate interplay observed in cuprates<sup>22–28</sup> and hole-doped nickelates such as

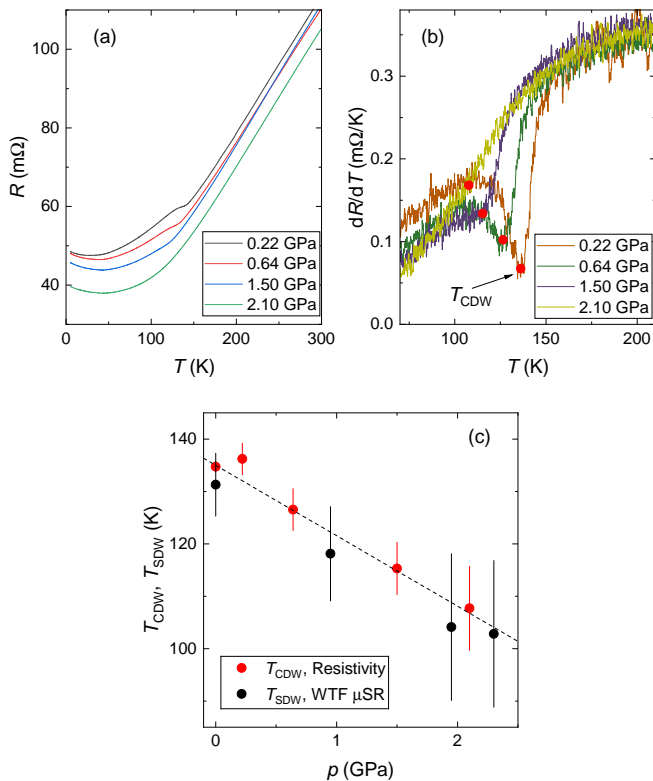


FIG. 7: **Pressure evolution of charge density wave (CDW) order.** (a) Temperature dependencies of resistivity  $R$  measured at pressures  $p = 0.22, 0.64, 1.50,$  and  $2.10$  GPa. (b) First derivatives of the resistivity curves. Red dots indicate the CDW transition temperature  $T_{\text{CDW}}$ . (c) Pressure dependencies of  $T_{\text{CDW}}$  and  $T_{\text{SDW}}$ . The solid line represents a linear fit to the  $T_{\text{CDW}}(p)$  data. Error bars for  $T_{\text{CDW}}$  represent uncertainties in determining the transition temperature.

$\text{La}_{2-x}\text{Sr}_x\text{NiO}_4$ <sup>30,31</sup>. In these systems, spin and charge orders are strongly intertwined and exhibit similar responses to external perturbations. However, open questions remain: Why does magnetic order changes from commensurate to incommensurate as one moves from the two-layer to the three-layer RP nickelate system? What drives the pressure-enhanced split of SDW and CDW transitions observed in  $\text{La}_3\text{Ni}_2\text{O}_7$  to the intertwined behavior seen in  $\text{La}_4\text{Ni}_3\text{O}_{10}$ ? Addressing these questions will require further experimental and theoretical investigations into the electronic structure and magnetic interactions of RP nickelates under varying conditions.

## METHODS

### A. Sample Preparation

The  $\text{La}_4\text{Ni}_3\text{O}_{10}$  polycrystalline sample was synthesized using a combination of mechano-synthesis and solid-state

reaction method, similar to that described in Ref. 11. The starting materials were  $\text{La}_2\text{O}_3$  (5N, Sigma-Aldrich) and NiO (4N8, Alfa Aesar). Prior to synthesis,  $\text{La}_2\text{O}_3$  and NiO were dried at  $1200^\circ\text{C}$  and  $280^\circ\text{C}$ , respectively, for 12 hours. Stoichiometric amounts of freshly dried  $\text{La}_2\text{O}_3$  (21.490 g, 65.96 mmol) and NiO (7.390 g, 10.0 mmol) were well mixed in RM 100 (Retsch®) mechanical mortar. The mixture of oxides was divided into two aliquots and placed together with 10 mm balls in a 45 ml agate grinding bowl and then subjected to mechano-synthesis in a PULVERISETTE 7 planetary micro ball-mill (Fritsch GmbH) during 20 cycles at 600 rpm for 5 min milling and 5 min cooling conditions. The resulting black precursor powder was cold-pressed into a pellet by applying 4000 bar uniaxial pressure and annealed in oxygen (5N, PabGas) under 200 ml/min flow at  $1100^\circ\text{C}$  for 10 h, followed by a final thermal treatment performed at  $500^\circ$  for 6 h.

### B. $\mu\text{SR}$ experiments

The ambient-pressure and high-pressure muon-spin rotation/relaxation ( $\mu\text{SR}$ ) experiments were conducted at the  $\pi\text{M}3$  and  $\mu\text{E}1$  beamlines at the Paul Scherrer Institute (PSI Villigen, Switzerland), using the dedicated GPS (General Purpose Surface, Ref. 47) and GPD (General Purpose Decay, Refs. 48,49) muon spectrometers. Quasi-hydrostatic pressures of up to  $\simeq 2.3$  GPa were generated using double-wall piston-cylinder clamp cells made of the nonmagnetic MP35N alloy<sup>48</sup>. The  $\mu\text{SR}$  data were analyzed using the MUSRFIT software package<sup>50</sup>. The  $\mu\text{SR}$  experiments were performed in two modes. In the first mode, zero-field (ZF)  $\mu\text{SR}$  measurements were conducted without applying an external magnetic field. In the second mode, a weak transverse field (WTF) was applied perpendicular to the initial muon-spin polarization.

### C. ZF- and WTF- $\mu\text{SR}$ data analysis procedure

The experimental  $\mu\text{SR}$  data were fitted using the following functional form:

$$A(t) = A_{0,s}P_s(t) + A_{0,bg}P_{bg}(t), \quad (2)$$

where the subscripts s and bg denote the sample and background contributions respectively, and  $A_0$  and  $P$  represent the initial asymmetry and the time evolution of the muon-spin polarization. The sample polarization function,  $P_s(t)$ , was further divided into magnetic (m) and nonmagnetic (nm) components, with corresponding weights  $f_m$  and  $1 - f_m$ . In experiments conducted on the low-background GPS muon spectrometer<sup>47</sup>, the background contribution was found to be negligible ( $A_{0,bg} \simeq 0$ ). In  $\mu\text{SR}$  experiments under pressure performed at GPD muon instrument<sup>48,49</sup>, the background arises from



muons stopped in the pressure cell walls and accounts for approximately 50% of the total  $\mu$ SR response.

In ZF- $\mu$ SR experiments, the magnetic (m) and non-magnetic (nm) contributions to the sample muon-spin polarization function  $P_s(t)$  were obtained as:

$$P_{s,m}(t) = \frac{2}{3} \sum_i f_i e^{-\lambda_{\tau,i} t} J_0(\gamma_{\mu} B_{\text{int},i} t) + \frac{1}{3} e^{-\lambda_L t}, \quad (3)$$

and

$$P_{s,nm}(t) = \frac{2}{3} (1 - \sigma_{\text{GKT}}^2 t^2) \exp\left[-\frac{\sigma_{\text{GKT}}^2 t^2}{2}\right] + \frac{1}{3}, \quad (4)$$

where  $J_0$  is the zeroth-order Bessel function,  $\gamma_{\mu} = 851.616$  MHz/T is the muon gyromagnetic ratio,  $\lambda$  represents the exponential relaxation rates,  $\sigma_{\text{GKT}}$  is the Gaussian Kubo-Toyabe relaxation rate, and  $f_i$ s are the volume fractions of individual magnetic components ( $\sum f_i = f_m$ ). The coefficients 2/3 and 1/3 account for powder averaging, with 2/3 of the muon spins precessing in internal fields perpendicular (transverse, T) to the field direction and 1/3 remaining parallel (longitudinal, L) to  $B_{\text{int},i}$ <sup>33-35,57</sup>.

The WTF sample response was modeled as:

$$P_s(t) = f_m \left[ \frac{2}{3} e^{-\lambda_{\tau} t} + \frac{1}{3} e^{-\lambda_L t} \right] + (1 - f_m) e^{-\sigma_{\text{WTF}}^2 t^2 / 2} \cos(\gamma_{\mu} B_{\text{WTF}} t + \phi), \quad (5)$$

where  $\phi$  is the initial phase of the muon-spin ensemble,  $B_{\text{WTF}} = 5$  mT is the weak transverse field, and  $\sigma_{\text{WTF}}$  is the Gaussian relaxation rate of the nonmagnetic component. The first term in Eq. 5 corresponds to Eq. 3, where, due to data binning, all oscillating components are combined into a single decay term. The second term describes muon-spin precession in  $B_{\text{WTF}}$  within the non-magnetic phase of the sample.

#### D. Muon stopping sites and dipole-field calculations

Muon stopping sites were calculated using a DFT+ $\mu$  approach<sup>51</sup> using the MuFinder application<sup>52</sup>. Density functional theory calculations were performed using the plane-wave pseudopotential code CASTEP<sup>53</sup>. The PBEsol functional<sup>54</sup> was used in all calculations. Calculations were converged to  $\sim 3$  meV/atom using a plane-wave cutoff of 800 eV and a  $3 \times 3 \times 3$   $k$ -point grid<sup>55</sup>. 54 calculations were performed, each where a muon was implanted randomly into a cell of approximately  $11 \times 11 \times 14$  Å. The atomic positions were subsequently allowed to relax until the energy and atomic positions had converged to better than  $2 \times 10^{-2}$  meV/atom and  $1 \times 10^{-3}$  Å respectively, and the maximum force on any atom was less than  $5 \times 10^{-2}$  eV/Å. The final muon positions were clustered using the MuFinder application to give the candidate muon stopping sites, which were subsequently used

in the MUESR code<sup>56</sup> to calculate the dipolar field at these sites for candidate magnetic structures. To capture the effect of an incommensurate magnetic structure, such as a spin density wave, many calculations with the initial phase of the magnetic structure varied were performed.

#### E. Neutron powder diffraction experiments

Neutron powder diffraction (NPD) experiments were carried out using the high-intensity cold neutron diffractometer DMC (neutron wavelength  $\lambda_n = 3.82$  Å) and the high-resolution thermal neutron diffractometer HRPT ( $\lambda_n = 2.45$  Å), both located at the spallation neutron source SINQ (PSI Villigen, Switzerland)<sup>44,45</sup>. A ca. 9 g sample was loaded into an 8-mm V-container for use in the measurements. The diffraction data were analyzed using the Rietveld refinement program Jana<sup>58,59</sup>.

#### F. Resistivity experiments

Experiments under ambient pressure were performed by using the ‘Resistivity’ option hardware and software of the Quantum Design Physical Property Measurement System (PPMS). Experiments under pressure were performed using the same PPMS instrument by using Almax EasyLab Pcell 15/30 module.<sup>60</sup>

#### G. Other experimental techniques

The specific heat measurements, were performed using the PPMS-9 (Physical Property Measurement System) at the Gdańsk University of Technology. Measurements were conducted using the ‘Heat Capacity’ option.

Laboratory x-ray powder diffraction was performed at room temperature in the Bragg-Brentano geometry using a Bruker AXS D8 Advance diffractometer (Bruker AXS GmbH, Karlsruhe, Germany) equipped with a Ni-filtered Cu  $K\alpha$  radiation and a 1D LynxEye PSD detector to confirm the phase-purity. Le Bail analysis of the obtained diffraction pattern was performed using the FullProf Suite package<sup>61</sup>.

Thermogravimetric Analysis (TGA) hydrogen reduction was performed to elucidate the oxygen content in the resulting  $\text{La}_4\text{Ni}_3\text{O}_{10-\delta}$  compound. The initial sample mass was 88.68 mg. A NETZSCH STA 449F1 Simultaneous Thermal Analyzer (STA) was used for the thermogravimetry experiment. The gas used in the experiment was a mixture of 5 vol.% of hydrogen (Messer Schweiz AG, 5N) in helium (PanGas, 6N).

#### DATA AVAILABILITY

All relevant data are available from the authors. The  $\mu$ SR data can also be found at the following link

<http://musruser.psi.ch/cgi-bin/SearchDB.cgi>.

## ACKNOWLEDGEMENTS

Z.G. acknowledges support from the Swiss National Science Foundation (SNSF) through SNSF Starting Grant (No. TMSGI2.211750). I.P. acknowledges financial support from Paul Scherrer Institute research grant No. 2021\_0134.

## AUTHORS CONTRIBUTIONS

R.K. conceived and supervised the project. D.J.G. and I.P. synthesized the sample and conducted x-ray and

thermogravimetry characterization. R.K. performed the ambient pressure and high pressure  $\mu$ SR experiments and analyzed the data. T.J.H. calculated the muon stopping sites and dipole-field distributions for various possible magnetic structures. I.P., L.K., and V.P. conducted the neutron powder diffraction experiments and analyzed the data. V.S. and Z.G. conducted electrical transport experiments under pressure with contribution from M.B. S.K., M.J.W., and T.K. conducted the specific heat experiments. R.K. and T.J.H. wrote the manuscript with contributions from I.P., T.K., D.J.G., J.A.K., H.L., and Z.G.

\* Electronic address: [rustem.khasanov@psi.ch](mailto:rustem.khasanov@psi.ch)

† Electronic address: [thomas.hicken@psi.ch](mailto:thomas.hicken@psi.ch)

‡ Electronic address: [igor.plokhikh@psi.ch](mailto:igor.plokhikh@psi.ch); [i.plokhikh@fz-juelich.de](mailto:i.plokhikh@fz-juelich.de)

- <sup>1</sup> Hualei Sun, Mengwu Huo, Xunwu Hu, Jingyuan Li, Zengjia Liu, Yifeng Han, Lingyun Tang, Zhongquan Mao, Pengtao Yang, Bosen Wang, Jinguang Cheng, Dao-Xin Yao, Guang-Ming Zhang, and Meng Wang, *Signatures of superconductivity near 80 K in a nickelate under high pressure*, Nature **621**, 493 (2023).  
<https://doi.org/10.1038/s41586-023-06408-7>
- <sup>2</sup> Junjie Zhang, D. Phelan, A.S. Botana, Yu-Sheng Chen, Hong Zheng, M. Krogstad, Suyin Grass Wang, Yiming Qi, J.A. Rodriguez-Rivera, R. Osborn, S. Rosenkranz, M.R. Norman, and J.F. Mitchell, *Intertwined density waves in a metallic nickelate*, Nat Commun. **11**, 6003 (2020).  
<https://doi.org/10.1038/s41467-020-19836-0>
- <sup>3</sup> Yinghao Zhu, Di Peng, Enkang Zhang, Bingying Pan, Xu Chen, Lixing Chen, Huifen Ren, Feiyang Liu, Yiqing Hao, Nana Li, Zhenfang Xing, Fujun Lan, Jiyuan Han, Junjie Wang, Donghan Jia, Hongliang Wo, Yiqing Gu, Yimeng Gu, Li Ji, Wenbin Wang, Huiyang Gou, Yao Shen, Tianping Ying, Xiaolong Chen, Wenge Yang, Huibo Cao, Changlin Zheng, Qiaoshi Zeng, Jian-gang Guo, and Jun Zhao Show, *Superconductivity in pressurized trilayer  $La_4Ni_3O_{10-\delta}$  single crystals*, Nature **631**, 531 (2024).  
<https://doi.org/10.1038/s41586-024-07553-3>
- <sup>4</sup> Hirofumi Sakakibara, Masayuki Ochi, Hibiki Nagata, Yuta Ueki, Hiroya Sakurai, Ryo Matsumoto, Kensei Terashima, Keisuke Hirose, Hiroto Ohta, Masaki Kato, Yoshihiko Takano, and Kazuhiko Kuroki, *Theoretical analysis on the possibility of superconductivity in the trilayer Ruddlesden-Popper nickelate  $La_4Ni_3O_{10}$  under pressure and its experimental examination: Comparison with  $La_3Ni_2O_7$* , Phys. Rev. B **109**, 144511 (2024).  
<https://doi.org/10.1103/PhysRevB.109.144511>
- <sup>5</sup> Meng Wang, Hai-Hu Wen, Tao Wu, Dao-Xin Yao, Tao Xiang, *Normal and superconducting properties of  $La_3Ni_2O_7$* , Chinese Physics Letters **41**, 077402 (2024).  
<https://doi.org/10.1088/0256-307X/41/7/077402>
- <sup>6</sup> Mingxin Zhang, Cuiying Pei, Xian Du, Weixiong Hu, Yantao Cao, Qi Wang, Juefei Wu, Yidian Li, Huanyu

- Liu, Chenhaoping Wen, Yi Zhao, Changhua Li, Weizheng Cao, Shihao Zhu, Qing Zhang, Na Yu, Peihong Cheng, Lili Zhang, Zhiwei Li, Jinkui Zhao, Yulin Chen, Hanjie Guo, Congjun Wu, Fan Yang, Shichao Yan, Lexian Yang, and Yanpeng Qi, *Superconductivity in trilayer nickelate  $La_4Ni_3O_{10}$  under pressure*, arxiv:231107423.  
<https://doi.org/10.48550/arXiv.2311.07423>
- <sup>7</sup> Guoqing Wu, J. J. Neumeier, and M. F. Hundley, *Magnetic susceptibility, heat capacity, and pressure dependence of the electrical resistivity of  $La_3Ni_2O_7$  and  $La_4Ni_3O_{10}$* , Phys. Rev. B **63**, 245120 (2001).  
<https://doi.org/10.1103/PhysRevB.63.245120>
- <sup>8</sup> Shangxiong Huangfu, Xiaofu Zhang, and Andreas Schilling, *Correlation between the tolerance factor and phase transition in  $A_{4-x}B_xNi_3O_{10}$  ( $A$  and  $B = La, Pr$ , and  $Nd$ ;  $x = 0, 1, 2, 3$ )*, Phys. Rev. Research **2**, 033247 (2020).  
<https://doi.org/10.1103/PhysRevResearch.2.033247>
- <sup>9</sup> Haoxiang Li, Xiaoqing Zhou, Thomas Nummy, Junjie Zhang, Victor Pardo, Warren E. Pickett, J. F. Mitchell, and D. S. Dessau, *Fermiology and electron dynamics of trilayer nickelate  $La_4Ni_3O_{10}$* , Nat. Commun. **8**, 704 (2017).  
<https://doi.org/10.1038/s41467-017-00777-0>
- <sup>10</sup> Junjie Zhang, Hong Zheng, Yu-Sheng Chen, Yang Ren, Masao Yonemura, Ashfia Huq, and J. F. Mitchell, *High oxygen pressure floating zone growth and crystal structure of the metallic nickelates  $R_4Ni_3O_{10}$  ( $R = La, Pr$ )*, Phys. Rev. Mater. **4**, 083402 (2020).  
<https://doi.org/10.1103/PhysRevMaterials.4.083402>
- <sup>11</sup> Rustem Khasanov, Thomas J. Hicken, Dariusz J. Gawryluk, Loic Pierre Sorel, Steffen Bötzel, Frank Lechermann, Ilya M. Eremin, Hubertus Luetkens, and Zurab Guguchia, *Pressure-Induced Split of the Density Wave Transitions in  $La_3Ni_2O_{7-\delta}$* , arXiv:2402.10485.  
<https://doi.org/10.48550/arXiv.2402.10485>
- <sup>12</sup> Ningning Wang, Gang Wang, Xiaoling Shen, Jun Hou, Jun Luo, Xiaoping Ma, Huaixin Yang, Lifan Shi, Jie Dou, Jie Feng, Jie Yang, Yunqing Shi, Zhian Ren, Hanming Ma, Pengtao Yang, Ziyi Liu, Yue Liu, Hua Zhang, Xiaoli Dong, Yuxin Wang, Kun Jiang, Jiangping Hu, Shoko Nagasaki, Kentaro Kitagawa, Stuart Calder, Jiaqiang Yan, Jianping Sun, Bosen Wang, Rui Zhou, Yoshiya Uwatoko,

- and Jinguang Cheng, *Bulk high-temperature superconductivity in pressurized tetragonal  $\text{La}_2\text{PrNi}_2\text{O}_7$* , *Nature* **634**, 579 (2024).  
<https://doi.org/10.1038/s41586-024-07996-8>
- <sup>13</sup> Mengzhu Shi, Di Peng, Kaibao Fan, Zhenfang Xing, Shaohua Yang, Yuzhu Wang, Houpu Li, Rongqi Wu, Mei Du, Binghui Ge, Zhidan Zeng, Qiaoshi Zeng, Jianjun Ying, Tao Wu, Xianhui Chen, *Superconductivity of the hybrid Ruddlesden-Popper  $\text{La}_5\text{Ni}_3\text{O}_{11}$  single crystals under high pressure*, arXiv:2502.01018v1.  
<https://doi.org/10.48550/arXiv.2502.01018>
- <sup>14</sup> Mingzhe Li, Jiashuo Gong, Yinghao Zhu, Ziyuan Chen, Jiakang Zhang, Enkang Zhang, Yuanji Li, Ruotong Yin, Shiyuan Wang, Jun Zhao, Dong-Lai Feng, Zengyi Du, Ya-Jun Yan, *Direct Visualization of an Incommensurate Unidirectional Charge Density Wave in  $\text{La}_4\text{Ni}_3\text{O}_{10}$* , arXiv:2501.18885v1.  
<https://doi.org/10.48550/arXiv.2501.18885>
- <sup>15</sup> Cuiying Pei, Mingxin Zhang, Di Peng, Shangxiong Huangfu, Shihao Zhu, Qi Wang, Juefei Wu, Zhenfang Xing, Lili Zhang, Yulin Chen, Jinkui Zhao, Wenge Yang, Hongli Suo, Hanjie Guo, Qiaoshi Zeng, Yanpeng Qi, *Pressure-Induced Superconductivity in  $\text{Pr}_4\text{Ni}_3\text{O}_{10}$  Single Crystals*, arXiv:2411.08677v1.  
<https://doi.org/10.48550/arXiv.2411.08677>
- <sup>16</sup> Enkang Zhang, Di Peng, Yinghao Zhu, Lixing Chen, Bingkun Cui, Xingya Wang, Wenbin Wang, Qiaoshi Zeng, Jun Zhao, *Bulk superconductivity in pressurized trilayer nickelate  $\text{Pr}_4\text{Ni}_3\text{O}_{10}$  single crystals*, arXiv:2501.17709v2.  
<https://doi.org/10.48550/arXiv.2501.17709>
- <sup>17</sup> Shangxiong Huangfu, Gawryluk Dariusz Jakub, Xiaofu Zhang, Olivier Blacque, Pascal Puphal, Ekaterina Pomjakushina, Fabian O. von Rohr, and Andreas Schilling, *Anisotropic character of the metal-to-metal transition in  $\text{Pr}_4\text{Ni}_3\text{O}_{10}$* , *Phys. Rev. B* **101**, 104104 (2020).  
<https://doi.org/10.1103/PhysRevB.101.104104>
- <sup>18</sup> Shangxiong Huangfu, Zurab Guguchi, Denis Cheptiakov, Xiaofu Zhang, Hubertus Luetkens, Dariusz Jakub Gawryluk, Tian Shang, Fabian O. von Rohr, and Andreas Schilling, *Short-range magnetic interactions and spin-glass behavior in the quasi-two-dimensional nickelate  $\text{Pr}_4\text{Ni}_3\text{O}_8$* , *Phys. Rev. B* **102**, 054423 (2020).  
<https://doi.org/10.1103/PhysRevB.102.054423>
- <sup>19</sup> M. D. Carvalho, M. M. Cruz, A. Wattiaux, J. M. Bassat, F. M. A. Costa, and M. Godinho, *Influence of oxygen stoichiometry on the electronic properties of  $\text{La}_x\text{Ni}_3\text{O}_{10\pm\delta}$* , *J. Appl. Phys.* **88**, 544 (2000).  
<https://doi.org/10.1063/1.373693>
- <sup>20</sup> D.-K. Seo, W. Liang, M.-H. Whangbo, Z. Zhang, and M. Greenblatt, *Electronic Band Structure and Madelung Potential Study of the Nickelates  $\text{La}_2\text{NiO}_4$ ,  $\text{La}_3\text{Ni}_2\text{O}_7$ , and  $\text{La}_4\text{Ni}_3\text{O}_{10}$* , *Inorg. Chem.* **35**, 6396 (1996).  
<https://doi.org/10.1021/ic960379j>
- <sup>21</sup> Jingyuan Li, Cui-Qun Chen, Chaoxin Huang, Yifeng Han, Mengwu Huo, Xing Huang, Peiyue Ma, Zhengyang Qiu, Junfeng Chen, Xunwu Hu, Lan Chen, Tao Xie, Bing Shen, Hualei Sun, Dao-Xin Yao, and Meng Wang, *Structural transition, electric transport, and electronic structures in the compressed trilayer nickelate  $\text{La}_4\text{Ni}_3\text{O}_{10}$* , *Sci. China-Phys. Mech. Astron.* **67**, 117403 (2024).  
<https://doi.org/10.1007/s11433-023-2329-x>
- <sup>22</sup> J. Tranquada, B. Sternlieb, J. Axe, Y. Nakamura, and S. Uchida, *Evidence for stripe correlations of spins and holes in copper oxide superconductors*, *Nature* **375**, 561 (1995).  
<https://doi.org/10.1038/375561a0>
- <sup>23</sup> G. Ghiringhelli, M. Le Tacon, M. Minola, S. Blanco-Canosa, C. Mazzoli, N. B. Brookes, G. M. De Luca, A. Frano, D. G. Hawthorn, F. He, T. Loew, M. M. Sala, D. C. Peets, M. Salluzzo, E. Schierle, R. Sutarto, G. A. Sawatzky, E. Weschke, B. Keimer, and L. Braicovich, *Long-range incommensurate charge fluctuations in  $(\text{Y,Nd})\text{Ba}_2\text{Cu}_3\text{O}_{6+x}$* , *Science* **337**, 821 (2012).  
<https://doi.org/10.1126/science.1223532>
- <sup>24</sup> J. Chang, E. Blackburn, A. T. Holmes, N. B. Christensen, J. Larsen, J. Mesot, R. Liang, D. A. Bonn, W. N. Hardy, A. Watenphul, M. von Zimmermann, E. M. Forgan, and S. M. Hayden, *Direct observation of competition between superconductivity and charge density wave order in  $\text{YBa}_2\text{Cu}_3\text{O}_y$* , *Nat. Phys.* **8**, 871 (2012).  
<https://doi.org/10.1038/NPHYS2456>
- <sup>25</sup> E. Fradkin, S. A. Kivelson, and J. M. Tranquada, *Colloquium: Theory of intertwined orders in high temperature superconductors*, *Rev. Mod. Phys.* **87**, 457 (2015).  
<https://doi.org/10.1103/RevModPhys.87.457>
- <sup>26</sup> B. Keimer, S. A. Kivelson, M. R. Norman, S. Uchida, and J. Zaanen, *From quantum matter to high-temperature superconductivity in copper oxides*, *Nature* **518**, 179 (2015).  
<https://doi.org/10.1038/nature14165>
- <sup>27</sup> S. A. Kivelson, I. P. Bindloss, E. Fradkin, V. Oganesyan, J. M. Tranquada, A. Kapitulnik, and C. Howald, *How to detect fluctuating stripes in the high-temperature superconductors*, *Rev. Mod. Phys.* **75**, 1201 (2003).  
<https://doi.org/10.1103/RevModPhys.75.1201>
- <sup>28</sup> Z. Guguchia, D. Das, C. N. Wang, T. Adachi, N. Kitajima, M. Elender, F. Brückner, S. Ghosh, V. Grinenko, T. Shiroka, M. Müller, C. Mudry, C. Baines, M. Bartkowiak, Y. Koike, A. Amato, J. M. Tranquada, H.-H. Klauss, C. W. Hicks, and H. Luetkens, *Using Uniaxial Stress to Probe the Relationship between Competing Superconducting States in a Cuprate with Spin-stripe Order*, *Phys. Rev. Lett.* **125**, 097005 (2020).  
<https://doi.org/10.1103/PhysRevLett.125.097005>
- <sup>29</sup> Alessandro Ricci, Nicola Poccia, Gaetano Campi, Shrawan Mishra, Leonard Müller, Boby Joseph, Bo Shi, Alexey Zozulya, Marcel Buchholz, Christoph Trabant, James C. T. Lee, Jens Viehhaus, Jeroen B. Goedkoop, Agustinus Agung Nugroho, Markus Braden, Sujoy Roy, Michael Sprung, and Christian Schüssler-Langeheine, *Measurement of Spin Dynamics in a Layered Nickelate Using X-Ray Photon Correlation Spectroscopy: Evidence for Intrinsic Destabilization of Incommensurate Stripes at Low Temperatures*, *Phys. Rev. Lett.* **127**, 057001 (2021).  
<https://doi.org/10.1103/PhysRevLett.127.057001>
- <sup>30</sup> Junjie Zhang, Yu-Sheng Chen, D. Phelan, Hong Zheng, M. R. Norman, and J. F. Mitchell, *Stacked charge stripes in the quasi-2D trilayer nickelate  $\text{La}_4\text{Ni}_3\text{O}_8$* , *Proc. Natl. Acad. Sci.* **113**, 8945 (2016).  
<https://doi.org/10.1073/pnas.1606637113>
- <sup>31</sup> Junjie Zhang, D. M. Pajerowski, A. S. Botana, Hong Zheng, L. Harriger, J. Rodriguez-Rivera, J. P. C. Ruff, N. J. Schreiber, B. Wang, Yu-Sheng Chen, W. C. Chen, M. R. Norman, S. Rosenkranz, J. F. Mitchell, and D. Phelan, *Spin Stripe Order in a Square Planar Trilayer Nickelate*, *Phys. Rev. Lett.* **122**, 247201 (2019).  
<https://doi.org/10.1103/PhysRevLett.122.247201>
- <sup>32</sup> P. Scherrer, *Bestimmung der Größe und der inneren Struktur von Kolloidteilchen mittels Röntgenstrahlen*, *Göttinger Nachrichten Math. Phys.* **2**, 98 (1918).

- <http://eudml.org/doc/59018>
- <sup>33</sup> Alex Amato and Elvezio Morenzoni, *Introduction to Muon Spin Spectroscopy. Applications to Solid State and Material Sciences*, Springer Nature (2024). <https://doi.org/10.1007/978-3-031-44959-8>
- <sup>34</sup> A. Yaouanc and P. D. de Réotier, *Muon Spin Rotation, Relaxation, and Resonance*, Oxford Science Publications, 2011.
- <sup>35</sup> S. J. Blundell, R. De Renzi, T. Lancaster, F. L. Pratt (eds.) *Muon spectroscopy. An introduction*, Oxford: Oxford University Press, 2022.
- <sup>36</sup> A. W. Overhauser, *Mechanism of antiferromagnetism in dilute alloys*, J. Phys. Chem. Solids **13**, 71 (1960). [https://doi.org/10.1016/0022-3697\(60\)90128-1](https://doi.org/10.1016/0022-3697(60)90128-1).
- <sup>37</sup> A. Schenck, D. Andreica, and F. N. Gygax, and H. R. Ott, *Extreme quantum behavior of positive muons in CeAl<sub>2</sub> below 1 K*, Phys. Rev. B **65**, 024444 (2001). <https://doi.org/10.1103/PhysRevB.65.024444>
- <sup>38</sup> A. Amato, P. Dalmas de Réotier, D. Andreica, A. Yaouanc, A. Suter, G. Lapertot, I. M. Pop, E. Morenzoni, P. Bonfà, F. Bernardini, and R. De Renzi, *Understanding the  $\mu$ SR spectra of MnSi without magnetic polarons*, Phys. Rev. B **89**, 184425 (2014). <https://doi.org/10.1103/PhysRevB.89.184425>
- <sup>39</sup> R. Khasanov, A. Amato, P. Bonfà, Z. Guguchia, H. Luetkens, E. Morenzoni, R. De Renzi, and N. D. Zhigadlo, *High-pressure magnetic state of MnP probed by means of muon-spin rotation*, Phys. Rev. B **93**, 180509(R) (2016). <https://doi.org/10.1103/PhysRevB.93.180509>
- <sup>40</sup> R. Khasanov, A. Shengelaya, D. Di Castro, E. Morenzoni, A. Maisuradze, I. M. Savić, K. Conder, E. Pomjakushina, A. Bussmann-Holder, and H. Keller, *Oxygen Isotope Effects on the Superconducting Transition and Magnetic States Within the Phase Diagram of Y<sub>1-x</sub>Pr<sub>x</sub>Ba<sub>2</sub>Cu<sub>3</sub>O<sub>7- $\delta$</sub>* , Phys. Rev. Lett. **101**, 077001 (2008). <https://doi.org/10.1103/PhysRevLett.101.077001>
- <sup>41</sup> H. Boller, and A. Kallel, *First order crystallographic and magnetic phase transition in CrAs*, Solid State Commun. **9**, 1699 (1971). [https://doi.org/10.1016/0038-1098\(71\)90344-9](https://doi.org/10.1016/0038-1098(71)90344-9)
- <sup>42</sup> Rustem Khasanov, Zurab Guguchia, Ilya Eremin, Hubertus Luetkens, Alex Amato, Pabitra K. Biswas, Christian Rüegg, Michael A. Susner, Athena S. Sefat, Nikolai D. Zhigadlo, and Elvezio Morenzoni, *Pressure-induced electronic phase separation of magnetism and superconductivity in CrAs*, Sci Rep **5**, 13788 (2015). <https://doi.org/10.1038/srep13788>
- <sup>43</sup> R. Fernandes, A. Chubukov, and J. Schmalian, *What drives nematic order in iron-based superconductors?*, Nature Phys. **10**, 97 (2014). <https://doi.org/10.1038/nphys2877>
- <sup>44</sup> P. Fischer, G. Frey, M. Koch, M. Könnecke, V. Pomjakushin, J. Schefer, R. Thut, N. Schlumpf, R. Bürge, U. Greuter, S. Bondt, and E. Berruyer, *High-resolution powder diffractometer HRPT for thermal neutrons at SINQ*, Physica B **276-278**, 146 (2000). [https://doi.org/10.1016/S0921-4526\(99\)01399-X](https://doi.org/10.1016/S0921-4526(99)01399-X)
- <sup>45</sup> J. Schefer, P. Fischer, H. Heer, A. Isacson, M. Koch, and R. Thut, *A versatile double-axis multicounter neutron powder diffractometer*, Nuclear Instruments and Methods in Physics Research Section A: Accelerators, Spectrometers, Detectors and Associated Equipment, **288**, 477 (1990). [https://doi.org/10.1016/0168-9002\(90\)90141-R](https://doi.org/10.1016/0168-9002(90)90141-R)
- <sup>46</sup> H. LaBollita, J. Kapeghian, M. R. Norman, A. S. Botana, *Electronic structure and magnetic tendencies of trilayer La<sub>4</sub>Ni<sub>2</sub>O<sub>10</sub> under pressure: Structural transition, molecular orbitals, and layer differentiation*, Phys. Rev. B **109**, 195151 (2024). <https://doi.org/10.1103/PhysRevB.109.195151>
- <sup>47</sup> A. Amato, H. Luetkens, K. Sedlak, A. Stoykov, R. Scheuermann, M. Elender, A. Raselli, and D. Graf, *The new versatile general purpose surface-muon instrument (GPS) based on silicon photomultipliers for  $\mu$ SR measurements on a continuous-wave beam*, Rev. Sci. Instrum. **88**, 093301 (2017). <https://doi.org/10.1063/1.4986045>
- <sup>48</sup> R. Khasanov, Z. Guguchia, A. Maisuradze, D. Andreica, M. Elender, A. Raselli, Z. Shermadini, T. Goko, F. Knecht, E. Morenzoni, and A. Amato, *High pressure research using muons at the Paul Scherrer Institute*, High Pressure Res. **36**, 140 (2016). <https://doi.org/10.1080/08957959.2016.1173690>
- <sup>49</sup> Rustem Khasanov, *Perspective on muon-spin rotation/relaxation under hydrostatic pressure*, J. Appl. Phys. **132**, 190903 (2022). <https://doi.org/10.1063/5.0119840>
- <sup>50</sup> A. Suter and B. Wojek, *Musrfit: A Free Platform-Independent Framework for  $\mu$ SR Data Analysis*, Phys. Procedia **30**, 69 (2012). <https://doi.org/10.1016/j.phpro.2012.04.042>
- <sup>51</sup> S. J. Blundell and T. Lancaster, *DFT+ $\mu$ : Density functional theory for muon site determination*, Appl. Phys. Rev. **10**, 021316 (2023). <https://doi.org/10.1063/5.0149080>
- <sup>52</sup> B. Huddart, A. Hernandez-Melian, T. Hicken, M. Gomilek, Z. Hawkhead, S. Clark, F. Pratt, and T. Lancaster, *MuFinder: A program to determine and analyse muon stopping sites*, Computer Physics Communications **280**, 108488 (2022). <https://doi.org/10.1016/j.cpc.2022.108488>
- <sup>53</sup> S. J. Clark, M. D. Segall, C. J. Pickard, P. J. Hasnip, M. I. Probert, K. Refson, and M. C. Payne, *First principles methods using CASTEP*, Zeitschrift für kristallographie-crystalline materials **220**, 567 (2005). <https://doi.org/10.1524/zkri.220.5.567.65075>
- <sup>54</sup> J. P. Perdew, A. Ruzsinszky, G. I. Csonka, O. A. Vydrov, G. E. Scuseria, L. A. Constantin, X. Zhou, and K. Burke, *Restoring the Density-Gradient Expansion for Exchange in Solids and Surfaces*, Phys. Rev. Lett. **100**, 136406 (2008). <https://doi.org/10.1103/PhysRevLett.100.136406>
- <sup>55</sup> H. J. Monkhorst, and J. D. Pack, *Special points for Brillouin-zone integrations*, Phys. Rev. B **13**, 5188 (1976). <https://doi.org/10.1103/PhysRevB.13.5188>
- <sup>56</sup> P. Bonfà, I. J. Onuorah, and R. De Renzi, *Introduction and a Quick Look at MUESR, the Magnetic Structure and mUon Embedding Site Refinement Suite*, JPS Conf. Proc. **21**, 011052 (2018). <https://doi.org/10.7566/JSPSCP.21.011052>
- <sup>57</sup> A. Schenck, *Muon Spin Rotation Spectroscopy: Principles and Applications in Solid State Physics*, Adam Hilger, Bristol, 1985.
- <sup>58</sup> Václav Petříček, Lukáš Palatinus, Jakub Plášil, and Michal Dušek, *Jana2020 – a new version of the crystallographic computing system Jana*, Z. Kristallogr. **238**, 271 (2023). <https://doi.org/10.1515/zkri-2023-0005>
- <sup>59</sup> Václav Petříček, Michal Dušek, and Lukáš Palatinus, *Crystallographic Computing System JANA2006: General features*, Z. Kristallogr. **229**, 345 (2014).



<https://doi.org/10.1515/zkri-2014-1737>

<sup>60</sup> <https://almax-easylab.com/product/easylab-pcell-15-30/>

<sup>61</sup> Juan Rodríguez-Carvajal, *Recent advances in magnetic*

*structure determination by neutron powder diffraction Author links open overlay panel*, *Physica B*: **192**, 55 (1993).  
[https://doi.org/10.1016/0921-4526\(93\)90108-I](https://doi.org/10.1016/0921-4526(93)90108-I)